

Article

Numerical Simulation and Application of a Channel Heat Sink with Diamond Ribs

Dongxu Zhang ^{1,2}, Guoqiang Liu ^{1,2}, Yongkang Lai ^{1,2}, Xiaohui Lin ^{3,4,*} and Weihuang Cai ^{5,*}

¹ School of Public Health, Xiamen University, Xiamen 361005, China; zhangdongxu@xmu.edu.cn (D.Z.); gzliuq@163.com (G.L.); djydb1999@gmail.com (Y.L.)

² State Key Laboratory of Molecular Vaccinology and Molecular Diagnostics, Xiamen 361005, China

³ School of Mechanical and Automotive Engineering, Xiamen University of Technology, Xiamen 361024, China

⁴ Xiamen Key Laboratory of Robot Systems and Digital Manufacturing, Xiamen 361024, China

⁵ School of Mechatronic Engineering and Automation, Shanghai University, Shanghai 200444, China

* Correspondence: xhxmut@163.com (X.L.); caiweihuang3@gmail.com (W.C.)

Abstract: This paper presents a channel radiator with ribbed ribs and primarily investigates the fluid flow and heat-transfer characteristics of the channel radiator. A three-dimensional numerical simulation of the radiator's pressure-drop and heat-transfer process was conducted using the finite volume method. A comparison between the experimental data and the simulation results demonstrates that the simulation in this paper is accurate, with a maximum error not exceeding 5%. Furthermore, the radiator was further subjected to geometric parameter studies, principally including the height ratio between the fins and the channel, the fin angle, and the spacing between the fins. The thermal resistance, Nusselt number, friction factor, and heat-transfer enhancement factor were calculated. The results indicate that if the geometric parameters are selected appropriately, the heat sink will enhance heat-transfer performance within an acceptable pressure drop. When the Reynolds number is greater than 507.5, the height ratio of 25%, the rib angle of 135°, and the rib spacing of 2.5 mm can be given priority. This heat sink is used in PCR devices, and experimental results show that the novel channel heat sink can meet the heat dissipation requirements of the TEC during the PCR process.

Keywords: rhombic rib; heat-transfer enhancement; channel radiator; numerical simulation



Citation: Zhang, D.; Liu, G.; Lai, Y.; Lin, X.; Cai, W. Numerical Simulation and Application of a Channel Heat Sink with Diamond Ribs. *Water* **2023**, *15*, 3677. <https://doi.org/10.3390/w15203677>

Academic Editor: Giuseppe Pezzinga

Received: 7 September 2023

Revised: 14 October 2023

Accepted: 17 October 2023

Published: 20 October 2023



Copyright: © 2023 by the authors. Licensee MDPI, Basel, Switzerland. This article is an open access article distributed under the terms and conditions of the Creative Commons Attribution (CC BY) license (<https://creativecommons.org/licenses/by/4.0/>).

1. Introduction

The rapid advancement of industry presents novel challenges and opportunities in various disciplines, such as semiconductors, integrated circuits, laser technologies, and more. The progress within these sectors potentially offers us highly integrated systems and miniaturized components or electronic devices. From a heat-transfer perspective, this developmental trajectory engenders an increase in the thermal flux density of systems, thereby leading to the generation of hot spots [1,2]. The reliability of electronic components is extraordinarily sensitive to operating temperatures, with research indicating that for every degree Celsius above the limit, the reliability of the component reduces by 5%. Consequently, to guarantee the performance of electronic systems and minimize the incidence of malfunctions, numerous scholars have concentrated their efforts on enhancing the system's cooling performance to eliminate thermal loads and prevent the emergence of hot spots [3,4]. Regarding cooling technologies, numerous advanced methods have emerged thus far, including micro heat pipes, jet impingement cooling, and ion wind cooling, to name a few [5]. In the 1980s, an innovative electronic cooling system—the microchannel heat sink—was proposed by Tuckerman and Pease. This heat sink demonstrated extraordinary cooling capabilities and, compared to other technologies, was cost-effective and also facilitated efficient heat dissipation [6]. From that point onwards, scholars have conducted extensive research on various types of microchannel heat sinks.

Unquestionably, microchannel heat sinks have found applications in numerous studies. For instance, Alihosseini et al. [7] proposed a PCR reaction device based on microchannel cooling. The study findings reveal that in such a device, cooling a saliva sample within the PCR wells requires merely 16.5 s, significantly reducing the time for DNA amplification while also occupying minimal space. Liu et al. [8] proposed a novel dendritic microchannel heat sink for cooling a single prismatic lithium battery. The performance of the lithium battery with the dendritic microchannel heat sink was studied both numerically and experimentally. Optimal geometric parameters were obtained through single-objective and multi-objective genetic algorithm optimizations based on numerical research results. The results demonstrate that the optimized structure possesses efficient heat dissipation performance, with the maximum temperature of the lithium battery only reaching 306.84 K. Lan et al. [9] proposed an aluminum microchannel cooling system, applying it to the study of temperature rise in a single prismatic lithium-ion battery under various discharge rates. The research findings corroborate that the microchannel cooling system can be employed in battery thermal management. This system is capable of reducing both the maximum temperature rise and the temperature disparity throughout the battery. Radwan et al. [10] proposed a microchannel heat sink filled with nanofluids for cooling concentrated photovoltaic systems. They established a comprehensive model including a thermal model of the photovoltaic layer and a thermal fluid dynamics model of two-phase flow in the microchannel heat sink, to estimate performance parameters through numerical simulation. The study findings indicate that this heat sink not only significantly reduces the temperature of the solar cells but also retains high electrical efficiency, thereby enhancing the overall efficiency of the system. Chen et al. [11] developed a temperature-equalizing plate (VC) with radial multi-arterial incursions into microchannels for the thermal management of high-power light-emitting diodes (LEDs). Experimental results reveal that, compared with traditional copper plates, the VC significantly enhances cooling capacity, reducing the substrate surface temperature of the LED module by 7–27%. The aforementioned studies demonstrate the substantial application value of microchannel heat sinks; thus, it is imperative to study microchannel radiators.

Pertaining to the heat sink channels themselves, it is indisputable that different channel shapes (including cross-sectional shapes and surface indentations or protrusions) yield distinct performance. Mohammed et al. [12] conducted a numerical study on the heat transfer and flow characteristics of a wavy microchannel heat sink. The results demonstrate that the heat-transfer performance of the wavy microchannel surpasses that of a straight microchannel with an identical cross-section. The pressure-drop loss in the wavy microchannel is considerably less than the enhancement achieved in heat transfer. Lin et al. [13] implemented improvements in the wavelength and amplitude of a wavy-channel heat sink. The study results indicate that the performance of the heat sink significantly improves when the wavelength of the wave unit decreases and the amplitude increases; the enhancement effect is even more pronounced when the absolute difference in wavelength or amplitude between two adjacent wave units increases. Mohammed et al. [14] studied the impact of different channel shapes, such as serrated, curved, and stepped microchannels, on the performance of heat sinks. The research results indicate that the serrated heat sink has the minimum temperature and the maximum heat-transfer coefficient. The pressure-drop loss of all channel shapes is higher than that of traditional straight heat sinks. The serrated heat sink has the maximum pressure drop, friction coefficient, and wall shear-stress values, followed by the curved and stepped shapes. Chai et al. [15] examined the fluid flow and heat-transfer characteristics of a microchannel heat sink with offset sectoral re-entrant cavities in the side walls. The research results show that the new heat sink enhances heat-transfer performance within an acceptable pressure drop. Lei Chai et al. [16] investigated the enhanced heat transfer of a microchannel heat sink with periodic expansion–contraction cross-sections using experimental and numerical methods. The research findings suggest that, compared with traditional straight-channel heat sinks, the newly proposed heat sink with periodic expansion–contraction cross-sections significantly

enhances heat-transfer capability, increasing the average Nusselt number by approximately 1.8 times.

Furthermore, it has been discovered that introducing some fins into the channel can enhance the performance of the heat sink. Li et al. [17] designed a double-layer pin-fin heat sink structure and analyzed the impact of geometric effects on thermodynamic performance. The results suggest that among pin-fin structures with circular, diamond, and rectangular cross-sections, the circular pin-fin displays the best overall performance and minimal thermal resistance. Li et al. [18] proposed a novel microchannel heat sink with triangular cavities and rectangular ribs (TC-RR) and examined the effects of relative rib width (α) and relative cavity width (β) on flow and heat-transfer performance. The research findings show that the thermal enhancement factor of the TC-RR microchannel with $\alpha = 0.3$ and $\beta = 2.24$ reaches 1.69 at $Re = 500$. Due to a more uniform base temperature, reduced irreversibility, and superior heat-transfer performance, the novel micro heat sink holds promising prospects in microelectronic cooling systems. Pan et al. [19] proposed a pin-fin staggered bifurcated microchannel (PFSMMC) heat sink. They analyzed the effects of the aspect ratio of the staggered distributor on the heat-transfer characteristics of the PFSMMC heat sink under various non-uniform heat source conditions. The results indicate that as the aspect ratio increases, the uniformity of the heated surface temperature decreases, but when the aspect ratio is 0.32, the maximum heated surface temperature is relatively lower. Feng et al. [20] designed a novel interrupted microchannel with dual circular pin fins (IMCDCP) in each microchamber. The analysis of geometric parameters demonstrates that the spacing between pin fins plays a crucial role in wall temperature uniformity, and an appropriate pin-fin height contributes to enhanced heat transfer and reduced pressure drop. Alihosseini et al. [21] designed a wavy microchannel heat sink with oblique slot fins, investigating the impact on the thermal performance of fins with a width of 250 and 125 μm . Furthermore, they studied the effect of spacing on heat transfer. The results show that the introduction of fins generated secondary flow, leading to the reformation of the thermal boundary layer at each fin location, thereby continuously shaping fluid flow. Mohamed Omri et al. [22] performed a three-dimensional numerical analysis of nanofluid-enhanced heat transfer in a micro heat exchanger with triangular fins. Modification of the heat-exchanger geometry in the z-direction was carried out to achieve a uniform wall temperature profile. It was found that the performance of the heat exchanger can be significantly improved by using CNT nanofluids and triangular fins. However, the thermal performance factor increases with the increase in CNT volume fraction and decreases with the height of the fins.

The above literature shows that the application of heat sinks is extremely wide, and their own geometric structures (including channel inserts) directly affect their performance. Therefore, it is very important to conduct geometric parameter research on heat sinks. Under specific conditions, a set or several sets of optimal parameters can be conveniently found through parameter research. These conditions can be a combination of one or several factors such as the uniformity of the base temperature of the heat sink, low overall fluid resistance in the channel, light weight, etc. Parameter analysis can also clearly reveal how geometric parameters affect the performance of the heat sink. In this article, a numerical study was conducted on a heat sink with diamond-shaped fins in the channel. The results under different Reynolds numbers were evaluated, and the effects of fin height, fin spacing, and the ratio of fin height to channel height were discussed in detail.

2. Model Description

2.1. Three-Dimensional Model

The heat sink is shown in Figure 1. The flow-channel heat sink and cover plate are made of highly conductive material (copper). The overall model is symmetrically distributed, there are 10 uniformly arranged channels in the flow-channel heat sink, and each channel contains uniformly arranged diamond-shaped fins. The total length and width of the flow-channel heat sink are 54 mm each; the bottom surface of the heat sink is used for thermal contact with the heat source; the channel height $H = 3$ mm, the channel

length $L = 42\text{ mm}$, and the channel width $W = 2\text{ mm}$; and the channel wall is uniformly arranged with triangles. The main structural parameters are: the angle α of the diamond-shaped fins, the spacing s between the fins, and the ratio β of the fin height to the channel height, where $\beta = h/H$. A seal ring is used at the junction of the flow cover plate and the channel heat sink to ensure that the cooling liquid does not leak. The entire structure can be locked by tightening the cover plate and the cover with bolts.

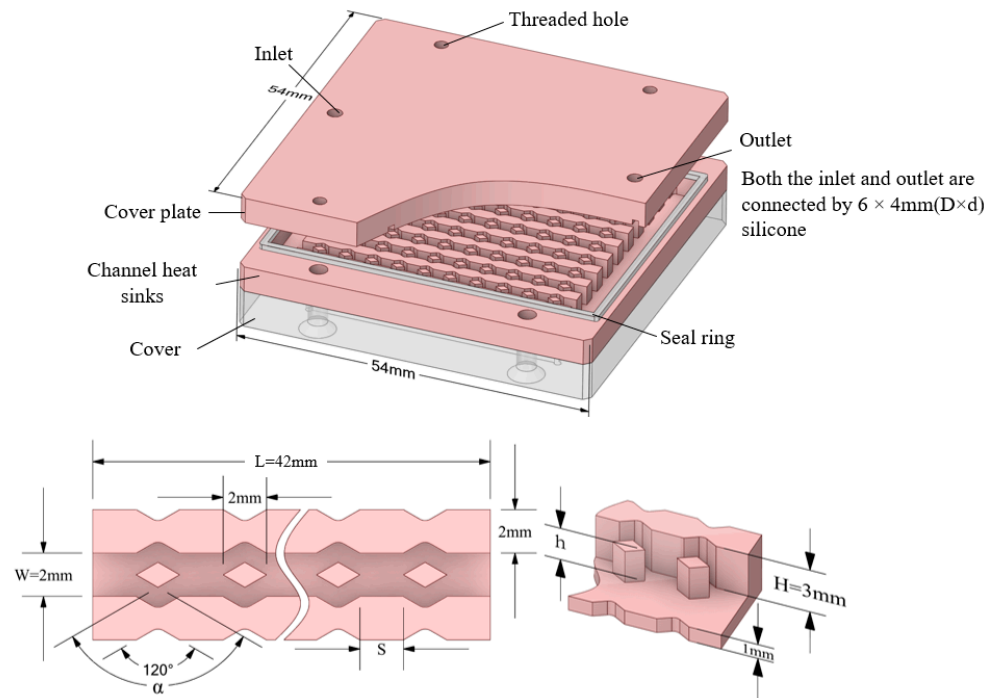


Figure 1. Overall schematic diagram of heat sink.

2.2. Computational Domain and Mathematical Model

In this work, the finite volume method is used to solve the fluid flow and heat transfer. The calculation domain is shown in Figure 2, and there is a 120 W heat source at the bottom of the channel radiator. The fluid medium is liquid water.

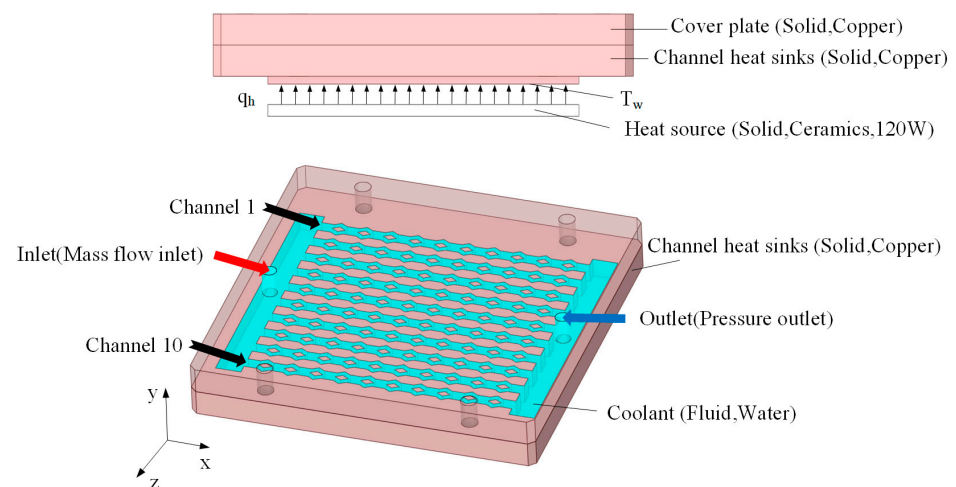


Figure 2. Computational domain.

To streamline the analysis, this study posits the following assumptions for the numerical simulation:

- The flow and heat-transfer processes are considered as steady-state;
- The fluid is incompressible and single-phase, and the thermal properties of fluid and solid are constant;
- The thermal resistance between solids is disregarded;
- Heat exchange between the exterior surface and its surroundings is not considered.

The conservation equation based on these assumptions is as follows:

Continuity equation [23]:

$$\frac{\partial u}{\partial x} + \frac{\partial v}{\partial y} + \frac{\partial w}{\partial z} = 0 \quad (1)$$

velocity components in x, y and z-directions are u, v and w, respectively.

Momentum in x-direction [24]:

$$\text{div}(\rho_f \mathbf{u}\mathbf{u}) = \text{div}(\mu_f \text{grad } u) - \frac{\partial p}{\partial x} \quad (2)$$

Similarly, the momentum equation in y- and z-directions can be written. Where \mathbf{u} is the velocity vector, p is the fluid pressure, ρ_f is the density of the fluid, μ_f is the dynamic viscosity of the fluid.

Energy equation for fluid domain is given by:

$$\text{div}(\rho_f \mathbf{u}T) = \text{div}\left(\frac{k_f}{C_{p,f}} \text{grad } T\right) \quad (3)$$

Energy equation for solid domain is given by:

$$\text{div}(k_s \nabla T) = 0 \quad (4)$$

where k_f and k_s are the thermal conductivities of the fluid and solid, respectively. T is temperature, $C_{p,f}$ is the specific heats of the fluid.

At the fluid–solid interface:

$$u = 0; T_f = T_s; -k_f \frac{\partial T_f}{\partial n} = -k_s \frac{\partial T_s}{\partial n} \quad (5)$$

where T_f and T_s are fluid temperature and solid temperature, respectively.

At inlet:

$$u = u_{in}; T = T_{in} \quad (6)$$

At bottom of the channel heat sink:

$$-k_s \left(\frac{\partial T_s}{\partial y}\right) = q_h \quad (7)$$

Where q_h originates from the heat source situated at the base.

At the outer wall:

$$\frac{\partial T_s}{\partial n} = 0 \quad (8)$$

2.3. Data Acquisition

Hydraulic diameter is the “characteristic length” used to calculate Reynolds number, Channel hydraulic diameter can be given by:

$$D_h = 2 \frac{HW}{H + W} \quad (9)$$

Inlet hydraulic diameter $D_h = d$.

The Reynolds number is a dimensionless number that can be used to characterize the flow of a fluid. The inlet Reynolds number is given by:

$$\text{Re} = \frac{\rho_f u_{in} D_h}{\mu_f} \quad (10)$$

where u_{in} is inlet velocity.

The apparent friction coefficient can be used to assess the resistance of water flowing through a channel, and is given by:

$$f = \frac{\Delta P D_h}{\rho_f L u_{in-c}^2} \quad (11)$$

where u_{in-c} represents the inlet velocity of the channel, while L denotes the channel's length. The pressure differential between the channel's inlet and outlet is represented by ΔP .

The thermal resistance as defined here is the ability of heatsink to resist heat transfer; it is given by:

$$R_t = \frac{T_{w,ave} - T_{in}}{Q} \quad (12)$$

where T_{in} is inlet temperature, $T_{w,ave}$ signifies the average temperature of the heated surface, and Q represents the quantity of heat.

The heat-transfer coefficient (h) indicates the amount of heat transferred by convection between a fluid and a solid surface. The Nusselt number (Nu) is the ratio of convective to conductive heat transfer across a boundary. They are given by:

$$h = \frac{Q}{A_{conv}(T_{w,ave} - T_{f,ave})} \quad (13)$$

$$\text{Nu} = \frac{h D_h}{k_f} \quad (14)$$

where A_{conv} is the contact area between the fluid and the solid for heat transfer, and $T_{f,ave}$ is the average temperature of the fluid in the channel.

The ratio of the heat-transfer area between the ribbed channel and the smooth, straight channel is given by:

$$\varepsilon = \frac{A_{conv}}{A_{smooth}} \quad (15)$$

where A_{smooth} represents the contact area within the smooth, straight channel where heat transfer takes place between the fluid and the solid.

According to the research of Karwa et al. [25] and Webb et al. [26], the heat-transfer enhancement factor η_f is utilized to evaluate the overall performance of the channel radiator. The heat-transfer enhancement factor simultaneously takes into account the heat dissipation capability and fluid flow capacity of the radiator. With this indicator, we can determine which parameter values can yield the greatest heat-transfer performance with the smallest pressure loss. The higher the heat enhancement coefficient, the better the overall performance of the microchannel radiator. The expression of η_f is given by:

$$P_{21} = \sum_1^n L/A' \quad (1)$$

$$\eta_f = \frac{\text{Nu}/\text{Nu}_0}{(f/f_0)^{1/3}} \quad (16)$$

where subscript 0 denotes the smooth, straight microchannel; thus, Nu/Nu_0 represents the relative Nusselt number. Similarly, f/f_0 represents the relative friction factor. If the value of η_f is less than one, it implies that the enhancement of heat-transfer performance is less than the pressure-drop penalty generated in its channel, and vice versa. In all designs of channel radiators, it is desired that heat-transfer enhancement exceeds the pressure-drop penalty. Evidently, this design poses a challenge; thus, it is also acceptable to improve heat-transfer performance with an acceptable pressure-drop penalty.

3. Experimental Device

As illustrated in Figure 3, the experimental setup comprises a direct current power source, a pump, a water bath, a data acquisition system, a pressure transducer, a control panel, a personal computer, an integrated heat sink, and a thermocouple assembly. The cover plate and channel heat sink are crafted from copper preforms in a single operation, thus negating the need for additional process treatments. A ceramic heating plate supplants traditional heating elements at the base of the radiator.

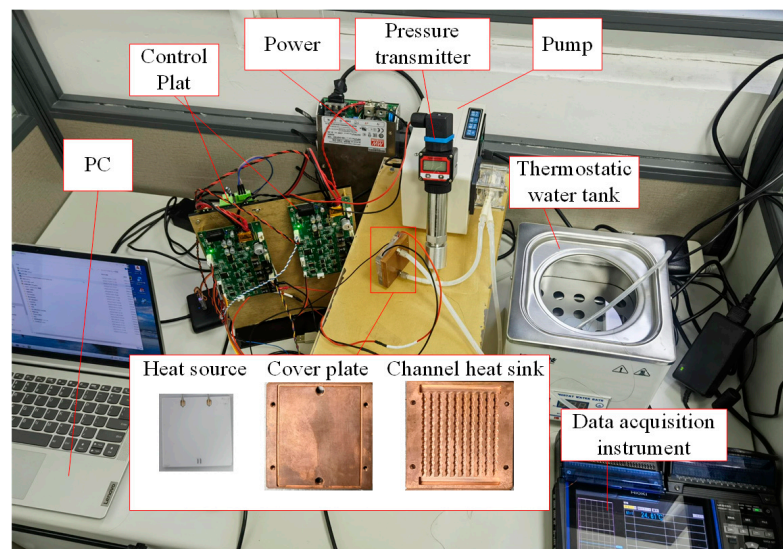


Figure 3. Experimental device.

As depicted in Figure 4, the computer, via the control plate, manages the power of the ceramic heating plate to emulate the heat generation of electronic devices. The interstice between the ceramic heating plate and the base surface is filled with thermal grease, mitigating the thermal resistance of component interconnections. A thermocouple, embedded within the central base surface of the channel heat sink and connected to the data acquisition system, procures the central base surface temperature, T_w . Water is introduced into the inlet of the channel heat sink through the operation of the pump, with its temperature maintained at an ideal ambient temperature (299.15 K) via the water bath. The inlet pressure P_1 is acquired through a pressure transducer connection, while the outlet pressure P_2 is at atmospheric levels. The overall pressure differential ΔP across the heat sink is determined by the subtraction of P_2 from P_1 .

The uncertainty in this work primarily stems from the precision of the machined parts, sensor accuracy, and instrument resolution. Errors predominantly comprise the thermocouple's uncertainty, part machining precision, pressure transmitter's resolution, data acquisition system's sampling accuracy, water bath's precision, and the direct current power supply's uncertainty. According to the studies of Pan et al. [27] and Taylor et al. [28], while each uncertainty in this study is small, the employment of multiple parameters in

calculations may instigate the propagation of uncertainty. The method of calculating error propagation is given by:

$$E_y = \sqrt{\sum_{i=1}^n \left(\frac{\partial Y}{\partial X_i} E_{X_i} \right)^2} \tag{17}$$

where Y is the calculated quantity, Xi is the actual measured value, and E_{Xi} is the uncertainty of the actual measured value. The values of the uncertainty are exhibited in Table 1.

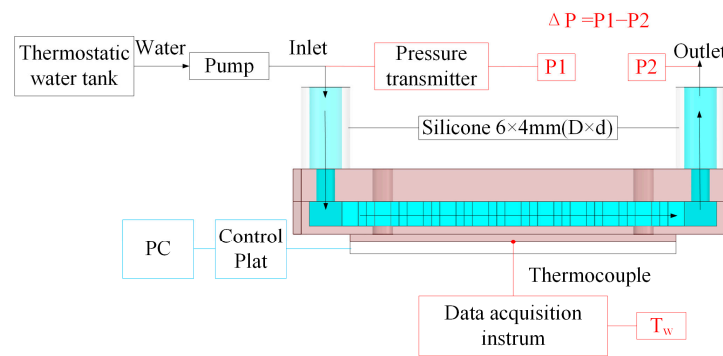


Figure 4. Experimental principle.

Table 1. Uncertainty.

Parameters	Uncertainty
Surface roughness (Channel heat sinks, Cover plate)	±2 μm
Thermostatic water tank	±0.5 K
Data acquisition instrument	0.1%
Power	1%
Thermocouple	±0.1 K
Pressure transmitter	0.5%

4. Result and Discussion

The influence of structural parameters on radiator performance is investigated through three-dimensional simulation. The total inlet Reynolds number is utilized as the abscissa, while the Nusselt number Nu, thermal resistance R_t, apparent friction factor f, and heat-transfer enhancement factor η_f are employed as output data. The range of variables is summarized in Table 2. Before analyzing the channel radiator’s performance, validation is required, including the accuracy of the simulation and grid independence.

Table 2. Geometric parameters and flow rates.

Variable	Value
Angle of diamond rib: α	90, 105, 120, 135, 150 (°)
The spacing of diamond rib: s	1, 1.5, 2, 2.5 (mm)
Ratio of rib height to channel height: β	25, 50, 75, 100 (%)
Inlet flow	60, 70, 80, 90, 100, 110, 120 (mL·min ⁻¹)

The computation is performed on a 6-core processor (CPU: Intel i5-10500 3.10 Ghz 6 cores 12 threads, RAM: 16 GB DDR4 2400 Mhz). The solving method employs the pressure-based SIMPLE algorithm, with pressure, momentum, and energy using a second-order upwind scheme. Convergence is considered achieved when the continuity and velocity residuals are less than 1 × 10⁻³, and the energy residual is less than 1 × 10⁻⁶. The physical parameters of materials are listed in Table 3.

Table 3. Material parameters.

Material	Density (kg·m ⁻³)	Specific Heat (J·kg ⁻¹ ·K ⁻¹)	Thermal Conductivity (W·m ⁻¹ ·K ⁻¹)	Viscosity (kg·m ⁻¹ ·s ⁻¹)
Ceramics	1345	710	150	-
Water	998.2	4182	0.6	0.001
Copper	8960	385	401	-

4.1. Validation

4.1.1. Validation of Grid Independence

As illustrated in Figure 5, polyhedral mesh division is carried out using Fluent. Mesh independence verification is performed on the flow-channel heat sink with $s = 2$ mm, $\alpha = 90^\circ$, and $\beta = 100\%$ (inlet flow rate of 120 mL·min⁻¹, water temperature of 299.15 K). The verification indices for mesh independence are the average temperature of the base surface ($T_{w,ave}$) and the pressure difference between the inlet and outlet of Channel 5 (ΔP_5).

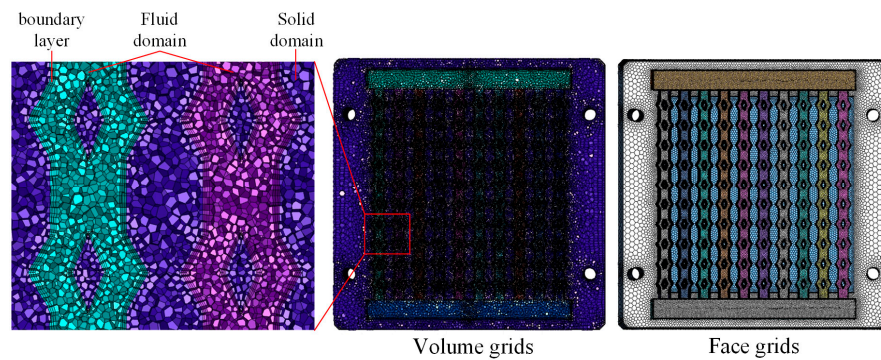


Figure 5. Computational grid of heat sink.

As shown in Figure 6, $T_{w,ave}$ and ΔP_5 decrease with the reduction of the maximum element size, stabilizing when the mesh size is less than 0.00225 m. Subsequently, as the mesh is refined, the deviations in $T_{w,ave}$ and ΔP_5 are both less than 5%. This agrees with the grid independence. After comprehensive consideration of simulation accuracy and calculation time, the maximum mesh size of 0.002 m was utilized for subsequent simulation research.

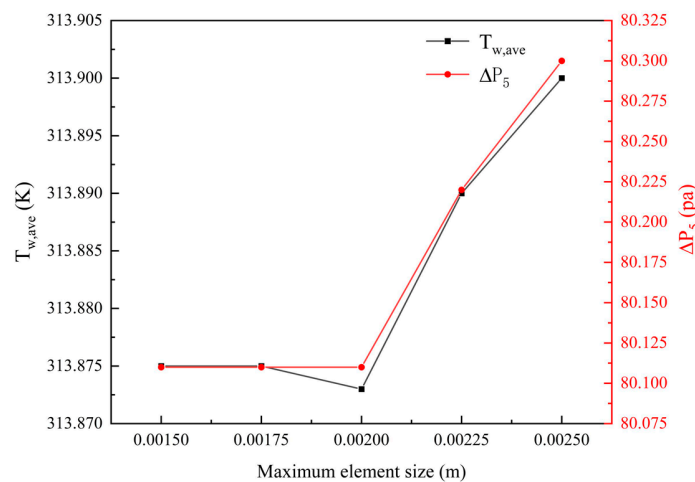


Figure 6. Grid independence verification.

4.1.2. Validation of Numerical Model

Experimental data were collected using the apparatus depicted in Figure 3, employing a flow channel radiator with parameters $s = 2$ mm, $\alpha = 120^\circ$, and $\beta = 100\%$ (inlet water

temperature of 299.15 K, inlet flow rates ranging from $100 \text{ mL}\cdot\text{min}^{-1}$ to $300 \text{ mL}\cdot\text{min}^{-1}$, and a flow rate gradient of $40 \text{ mL}\cdot\text{min}^{-1}$). The central temperature of the base surface of the flow channel radiator T_w and the overall pressure difference ΔP were taken as the verification indicators. The results shown in Figure 7 reveal that the experimental and simulated values of ΔP are very close across each Reynolds number gradient. However, the simulated values of T_w are consistently lower than the experimental values for each Reynolds number gradient. This discrepancy is attributed to the fact that in the simulation model, the heat source and flow channel radiator are regarded as ideally connected, thus rendering a heat-transfer capability that is somewhat higher than actuality, leading to slightly lower simulated values. The overall maximum error does not exceed 5%. Considering the verification results for both ΔP and T_w , the modeling and simulation of the flow channel radiator in this study are effective and suitable for subsequent simulation research.

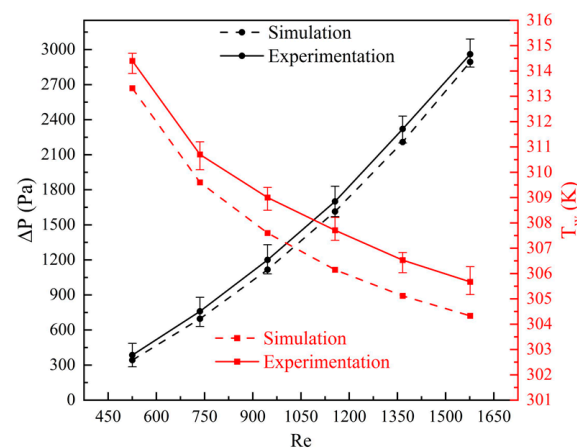


Figure 7. Validation of numerical model.

4.2. The Characteristics of the Radiator

For a flow channel radiator with parameters $s = 2 \text{ mm}$, $\alpha = 150^\circ$, and $\beta = 100\%$, a simulation was conducted at a flow rate of $60 \text{ mL}\cdot\text{min}^{-1}$ to study the radiator's characteristics. The simulated cloud diagrams were extracted at the cross-section $H/2$, and the results are presented in Figure 8a–c. The temperature of the cross-section, the pressure of the channels, and the velocity of the fluid within the channels all exhibit symmetric distribution. Channels closer to the center exhibit higher velocity, carrying away more heat but also manifesting increased pressure. Vortices appear at the four corners of the radiator. As these are distant from the heat-exchange area, they do not impact the cooling performance.

Due to the symmetry of the radiator's overall structure and the identical geometric parameters (s , α , and β) in each channel, the distribution of water flow to every channel is symmetrical, resulting in the evaluation indicators for all channels being symmetrical as well. The apparent friction factor and Nusselt numbers for each channel are illustrated in Figure 9a,b, respectively. It is evident that the central channel exhibits the lowest apparent friction factor and Nusselt number, while the values for the other channels demonstrate varying degrees of increase. In the smooth, straight channels and the new channels, the apparent friction factor values for channels 5 and 6 are exceedingly close, leading to their having the lowest and equal heat-transfer enhancement factors among all channels. In consideration of the radiator's symmetry and the minimal heat-transfer enhancement factor in the central channel, subsequent simulations will extract the Nusselt number, thermal resistance, apparent friction factor, and heat-transfer enhancement factor of channel 5 as output data.

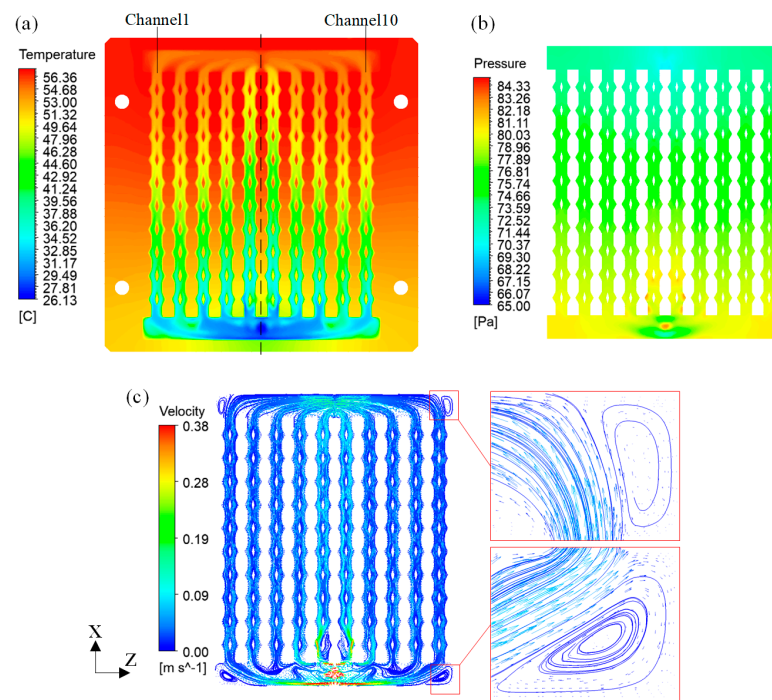


Figure 8. The simulation result: (a) Temperature; (b) Pressure; (c) Velocity.

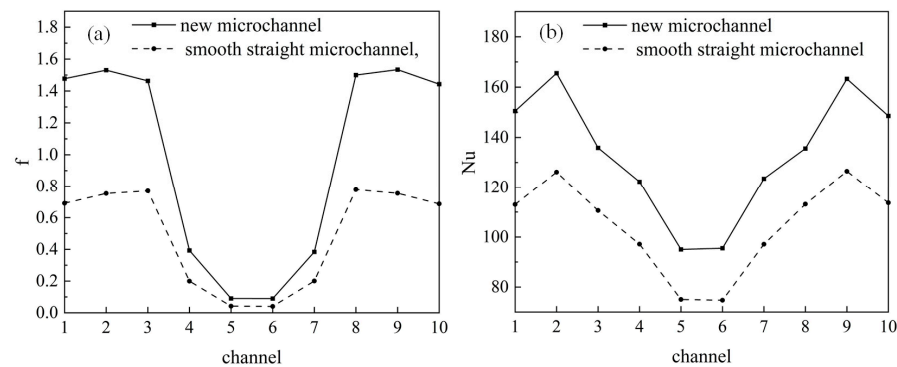


Figure 9. The characteristics of heat sink: (a) The apparent friction factor for each channel; (b) The Nusselt numbers for each channel.

4.3. The Impact of Geometric Parameters on the Heat Sink

4.3.1. Effects of Fin Angle α

Figure 10 shows the effect of design variable α on the performance of channel when the other design variables are kept constant ($\beta = 100\%$, $s = 2$). Figure 10a displays the thermal resistance R_t at various Reynolds numbers Re and different fin angles. The thermal resistance R_t of the radiator is lower under all fin angles compared to the smooth, straight channels, indicating that the ridged fins within the channels effectively enhance heat transfer. As the fin angle decreases and the Reynolds number increases, thermal resistance gradually diminishes. The primary reasons for this can be explained by the velocity of the water flow and the heat-transfer surface area ratio ϵ between the new channels and the straight channels. As the fin angle decreases, ϵ increases, signifying a larger exchange area between the fluid and the solid, thereby improving the heat-transfer capability. On the other hand, when the Re increases and the fin angle decreases, the average fluid velocity within the channel rises. Considering the aforementioned factors, thermal resistance gradually decreases, and the channel radiator exhibits the lowest thermal resistance when $\alpha = 90^\circ$.

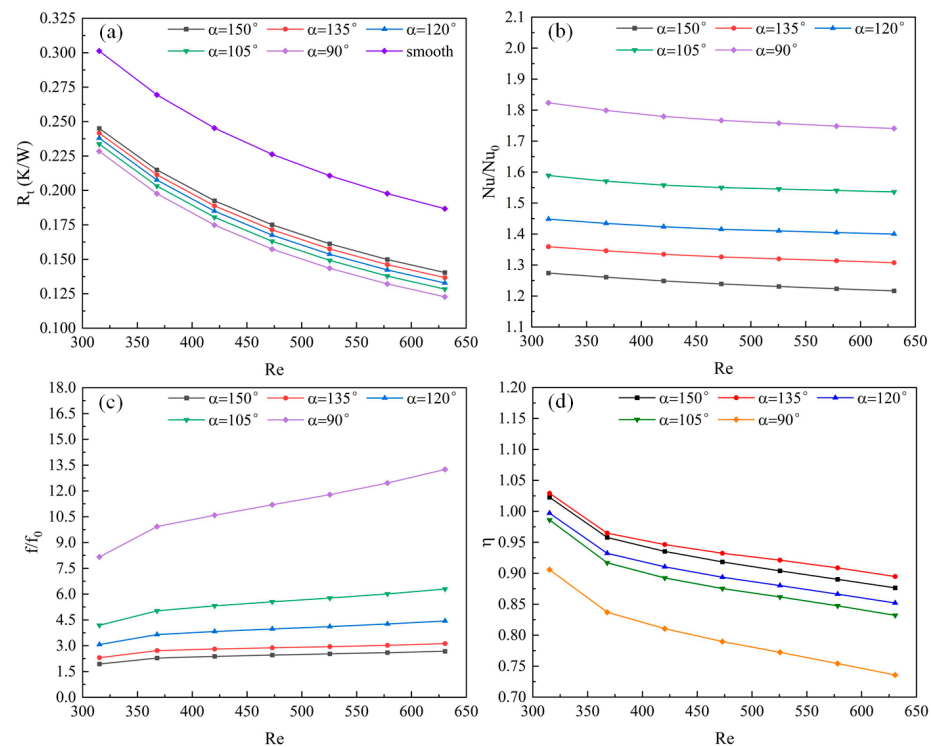


Figure 10. The influence of α on thermal hydraulic performance for the channel: (a) Thermal resistance; (b) Nusselt numbers ratio; (c) Apparent friction factor ratio; (d) Heat-transfer enhancement factor.

Figure 10b illustrates the Nusselt number ratio Nu/Nu_0 at various Reynolds numbers and different fin angles α . The Nusselt numbers under all fin angles are greater than those in smooth, straight channels. This is because the fins disturb the fluid's velocity, exerting a perturbing effect on the fluid regardless of the fin angle. The disturbance is weakest, and the heat-exchange area between the fluid and the solid is minimal when $\alpha = 150^\circ$, resulting in the lowest Nu/Nu_0 . From the perspective of Nusselt numbers, the heat-transfer performance is superior at $\alpha = 90^\circ$ compared to smooth, straight channels, reaching up to 1.82 when $Re = 315.32$.

Figure 10c exhibits the relative friction factor f/f_0 at various Reynolds numbers and different fin angles α . It can be observed that regardless of the fin angle, the fluid flow resistance within the channels is higher than that in smooth, straight channels, and it increases with the Reynolds number. When Re remains constant, the variation in fin angle has a dramatic effect on flow resistance and increases sharply as the fin angle decreases. At $\alpha = 90^\circ$ and $Re = 630.64$, f/f_0 is 13.25, indicating that the flow resistance is 13.25 times that of smooth, straight channels. This signifies a marked deterioration in flow performance, primarily due to an excessive pressure difference in the channel when $\alpha = 90^\circ$. Therefore, excessively small fin angles should be avoided in the current design. Angles of $\alpha = 150^\circ$ and $\alpha = 135^\circ$ may be prioritized, as they result in a flow resistance no more than three times that of smooth, straight channels.

Figure 10d shows the heat-transfer enhancement factor η_f at various Reynolds numbers and different fin angles α . η_f decreases with increasing Re across all angles, signifying that the radiator's overall performance is better at lower flow rates. When Re remains constant, η_f first increases and then decreases with the reduction of the fin angle. At $\alpha = 90^\circ$, η_f is at its lowest, where the pressure-drop penalty far outweighs the heat-transfer enhancement, resulting in η_f being only 0.74 at $Re = 630.64$. Therefore, in the current design, angles of $\alpha = 150^\circ$ or $\alpha = 135^\circ$ should preferably be utilized.

4.3.2. Effects of Height Ratio β

When $s = 2$ and $\alpha = 120^\circ$ and they remain constant, the influence of the design variable β on channel performance is illustrated in Figure 11. Figure 11a depicts the thermal resistance R_t at various Re and different height ratios. From the graph, it can be distinctly observed that the thermal resistance of all channels with different rib heights is lower than that of the smooth, straight channels, and furthermore, it diminishes gradually with the increase in Re . When the Re is constant, R_t first decreases with the increase in β , eventually stabilizing. The reason for this may be that when $\beta = 75\%$, it already provides a sufficiently large heat-transfer area, and even if β further increases to 100%, the resultant enhancement in heat-exchange performance will not increase substantially.

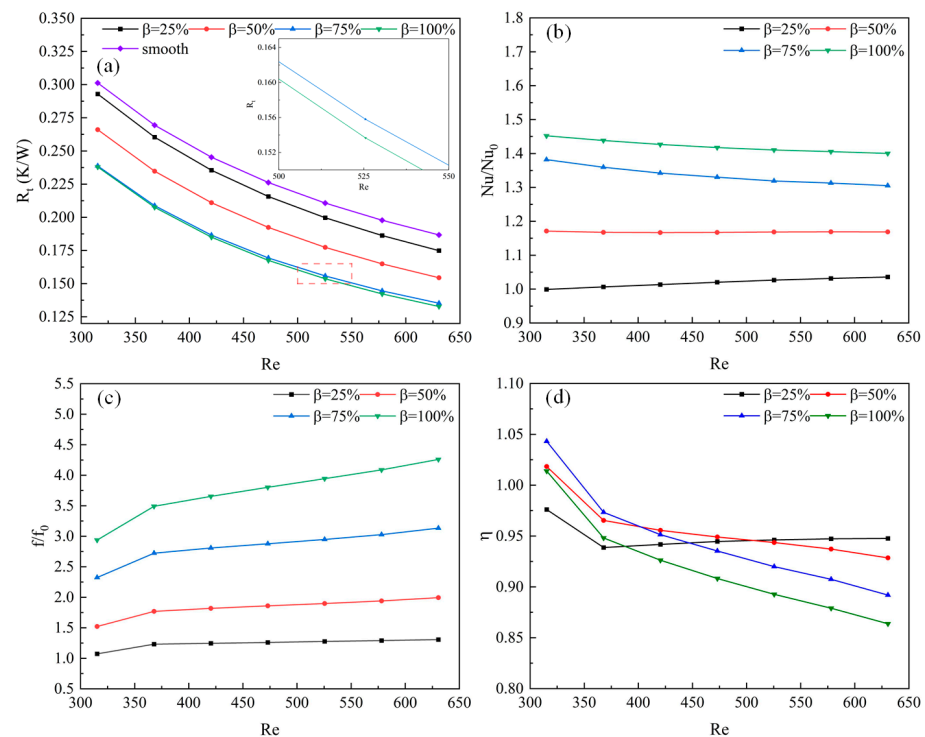


Figure 11. The influence of β on thermal hydraulic performance for the channel: (a) Thermal resistance; (b) Nusselt numbers ratio; (c) Apparent friction factor ratio; (d) Heat-transfer enhancement factor.

Figure 11b exhibits the Nusselt number ratio Nu/Nu_0 at various Re and different height ratios. When $\beta = 75\%$ and 100% , Nu/Nu_0 tends to decrease with the increase in Re , whereas when $\beta = 25\%$ and 50% , Nu/Nu_0 exhibits an ascending trend with the growth of Re . When Re remains constant, Nu/Nu_0 gradually increases with the enhancement of β . The reason for this could be the amplification of the heat-exchange area between the fluid and the solid as β grows, coupled with the fact that a larger β results in an increased ability of the ribs to disturb the fluid. Therefore, compared to the smooth, straight channels, the heat-transfer performance of the radiator is optimal when $\beta = 100\%$, with Nu/Nu_0 consistently exceeding 1.4.

Figure 11c demonstrates the relative friction factor f/f_0 at diverse Re and different height ratios, revealing that the fluid flow resistance within channels at all height ratios surpasses that of the smooth, straight channels. When $\beta = 75\%$ and 100% , f/f_0 progressively escalates with the increase in Re ; in contrast, when $\beta = 25\%$ and 50% , f/f_0 exhibits a tendency to stabilize with the growth of Re . This phenomenon might be attributed to the comparatively small pressure differential in the channels when $\beta = 25\%$ and 50% . Under the prevailing conditions, f/f_0 signifies that any value of β will influence flow performance; however, compared to smooth, straight channels, at $\beta = 25\%$ and 50% , f/f_0 does not exceed 2. Hence, in the current design, consideration can be prioritized for $\beta = 25\%$ and 50% .

Figure 11d portrays the heat-transfer enhancement factor η_f at various Re and different height ratios. With the exception of $\beta = 25\%$, all heat-transfer enhancement factors diminish with the growth in Re. The rate of reduction for the heat-transfer enhancement factor at $\beta = 50\%$ is markedly attenuated compared to $\beta = 75\%$ and 100% , whereas at $\beta = 25\%$, η_f initially declines and then steadily ascends with the increase in Re, and when $Re > 507.5$, its curve becomes the highest. In summary, if $Re > 507.5$, a preference for $\beta = 25\%$ is recommended; if $Re < 507.5$, a priority for $\beta = 50\%$ and 75% is advised.

4.3.3. Effects of Rib Space s

When $\beta = 100\%$ and $\alpha = 120^\circ$ and they remain constant, the influence of the design variable s on channel performance is illustrated in Figure 12. Figure 12a reveals the thermal resistance R_t at varying rib spacings. It is salient that the thermal resistance of the radiators at all rib spacings is inferior to that of the smooth, straight channels, and all the curves are closely congruent. The reason for this is that the alteration in rib spacing nearly fails to modify the ratio of the heat-transfer area between the new channel and the straight channel, thus resulting in equivalent heat-transfer characteristics.

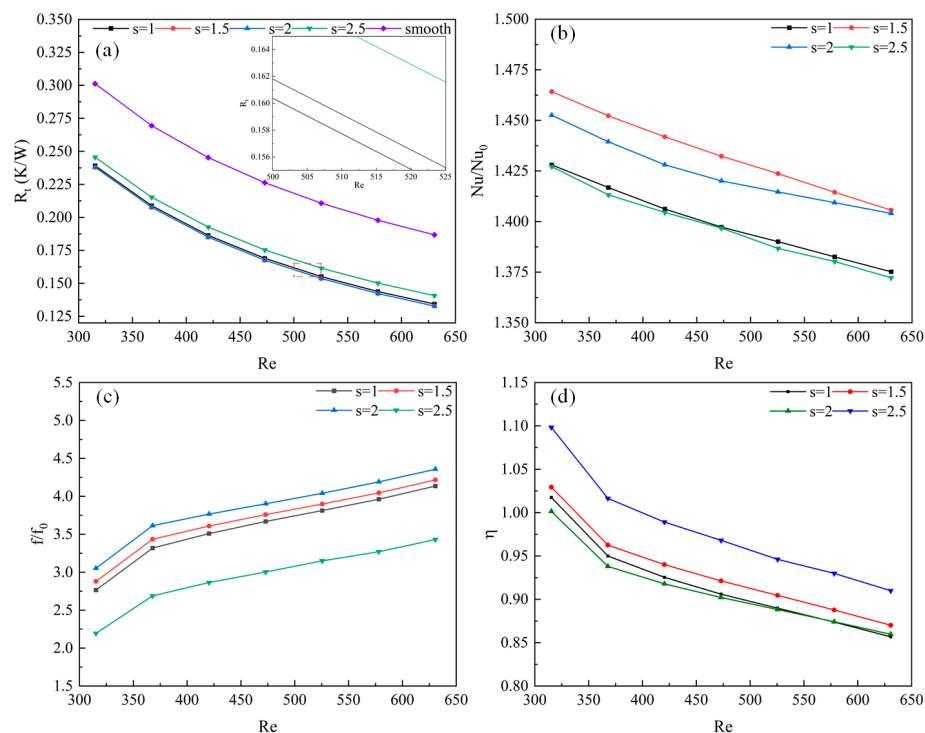


Figure 12. The influence of s on thermal hydraulic performance for the channel: (a) Thermal resistance; (b) Nusselt numbers ratio; (c) Apparent friction factor ratio; (d) Heat-transfer enhancement factor.

Figure 12b illustrates the Nusselt number ratio Nu/Nu_0 at different Re and different rib spacings. Aside from when $s = 2$, Nu/Nu_0 noticeably declines with an increase in Re, reaching its maximum when $s = 1.5$. Nu/Nu_0 at $s = 1$ and 2.5 are minimal and nearly identical. However, when $s = 2$, the rate of decrease in Nu/Nu_0 lessens when Re exceeds 472.98, and according to the current trend, it can be estimated that Nu/Nu_0 will become the greatest when Re surpasses 630.64 at $s = 2$. In summary, the heat-transfer performance is substantially reduced as Re increases.

Figure 12c depicts the relative friction factor f/f_0 at various Re and different rib spacings. It can be discerned that regardless of the spacing of the ribs, the fluid flow resistance within the channel is higher than that in a smooth, straight channel, and it increases with the enhancement of Re. When Re remains constant, f/f_0 initially rises with an increase in s and subsequently diminishes, reaching its minimum when $s = 2.5$; hence, in the present design, a preference may be given to $s = 2.5$. Furthermore, the graph reveals

that when $s = 1, 1.5,$ or $2,$ the trends of their curves are consistent and the values differ insignificantly, which could be attributed to the degree of disturbance to the fluid in the channel being almost the same under current conditions.

Figure 12d illustrates the heat-transfer enhancement factors η_f at varying Re and different rib spacings. All the curves exhibit a similar trend, with a maximum observed when $s = 2.5.$ Overall, it can be anticipated that when Re exceeds $630.64,$ the heat-transfer enhancement factor will rapidly diminish following the current trend.

4.4. The Application of Heat Sinks

Based on the analysis from the previous section, conclusions can be drawn as follows:

1. $\alpha = 150^\circ$ or $\alpha = 135^\circ$ is appropriate; 2. If $Re > 507.5,$ the preference should be given to $\beta = 25\%,$ whereas if $Re < 507.5,$ the preference should be given to $\beta = 50\%$ and $75\%;$
3. $s = 2.5$ may be considered with priority.

The channel heat sink studied in this article is used in PCR reaction devices, as shown in Figure 13. A thermoelectric cooler (TEC) is controlled programmatically to generate the temperatures required for the PCR process, and the TEC working face transmits this temperature to the biological reaction chamber through a heat-conducting sheet, ultimately facilitating the liquid within the reaction chamber to complete DNA amplification. The surface temperature requirements for a thermal conducting sheet are: generating a cyclical temperature of $328.15 \pm 3 \text{ K}$ to $368.15 \pm 3 \text{ K}$ (45 cycles, with the maximum exceeding 365.15 K and the minimum falling below 328.15 K), and a rate of temperature rise or fall not less than $5 \text{ K/s}.$ Owing to the characteristics of the TEC, when the working face is heated, the opposite side must be cooled, and the cooling capability is determined by the heat dissipation capacity of the channel heat sinks.

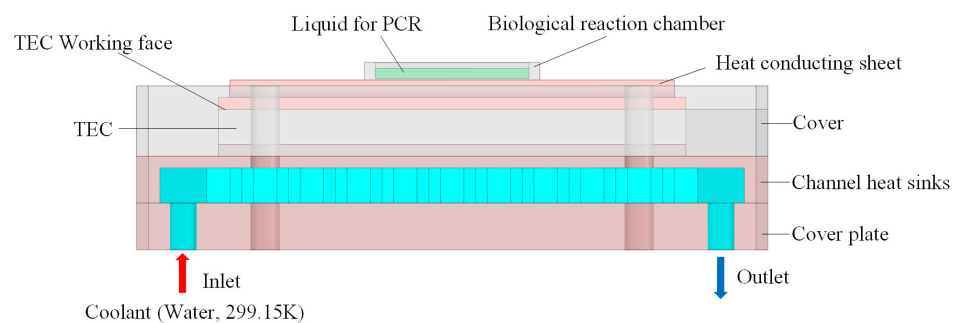


Figure 13. Application of heat sinks.

In practical testing, we utilized a channel heat sink with $\alpha = 135^\circ,$ $\beta = 25\%,$ and $s = 2.5,$ conducting tests at a flow rate of $100 \text{ mL} \cdot \text{min}^{-1}$ ($Re = 525.53$) and water temperature of $299.15 \text{ K}.$ The measuring apparatus was based on the experimental setup shown in Figure 3, using a data acquisition instrument to capture the temperature of the heat-conducting sheet surface (the contact face between the heat-conducting sheet and the biological reaction chamber, TH), as depicted in Figure 14. The test results indicated that the surface temperature of the heat-conducting sheet nearly reached 368.15 K at its peak during each cycle, with the minimum consistently below $328.15 \text{ K};$ the heating rate reached $7.9 \text{ K/s},$ and the cooling rate achieved $7.8 \text{ K/s}.$ Under these temperature conditions, the PCR reaction could be completed. Overall, this channel heat sink is capable of fulfilling the heat dissipation requirements. The symbol "..." shown in Figure 14 indicates that the rest of the curve is the same as the current curve for 45 cycles.

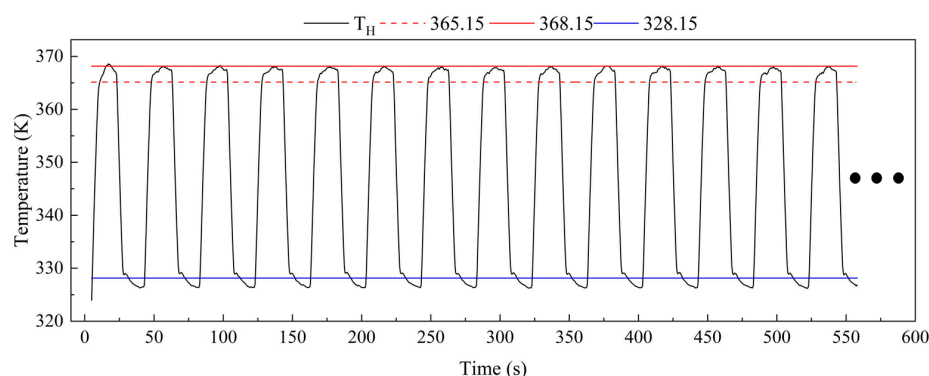


Figure 14. Temperature of the heat-conducting sheet surface, T_H .

5. Conclusions

In this paper, a simulation study was conducted on the fluid flow and heat-transfer characteristics of a channel heat sink with rhombic fins. The computed results were compared to the actual measured data, confirming that the computational error did not exceed 5%. An in-depth analysis of this radiator was carried out, with an extensive exploration of the influence of the fin's geometric shape on its thermal and hydraulic performance. The aim was to identify the optimal geometric parameters that enhance heat transfer without incurring significant pressure-drop penalties. Finally, the practical application of the radiator was introduced. The principal findings of this paper can be summarized as follows:

1. The angle of the rhombic fins within the channel has a substantial impact on the flow characteristics. When Re remains constant, the flow resistance at $\alpha = 90^\circ$ is 13.25 times that of a smooth, straight channel, resulting in a pressure-drop penalty that far outweighs the enhancement in heat transfer. Considering both flow and heat-transfer characteristics, the optimal choices are $\alpha = 150^\circ$ or $\alpha = 135^\circ$.
2. With Re held constant, the thermal resistance decreases as β increases. At $\beta = 25\%$ and 50% , f/f_0 does not exceed 2. Weighing both flow and heat-transfer characteristics, in the current design, $\beta = 25\%$ and 50% may be considered. If $Re > 507.5$, the preference should be given to $\beta = 25\%$, whereas if $Re < 507.5$, the preference should be given to $\beta = 50\%$ and 75% .
3. The influence of the design variable s on channel performance indicates that, in the current design, priority can be given to $s = 2.5$, in which case f/f_0 is the lowest and the heat-transfer enhancement factor is the highest.
4. This channel radiator is employed in PCR devices. Actual experimental results indicate that the radiator can furnish an ample amount of heat-exchange capacity, enabling the TEC to produce a stable cyclical temperature.

Author Contributions: Software, Y.L.; Validation, W.C.; Formal analysis, D.Z.; Investigation, D.Z.; Writing original draft, G.L.; Visualization, W.C.; Supervision, X.L. All authors have read and agreed to the published version of the manuscript.

Funding: This research was funded by National Natural Science Foundation of China (62003284); The Science and Technology Projects of Fujian Province, China (2021Y0093); Natural Science Foundation of Fujian Province, China (2021J011200); Study on the Correlation between Vitamin A and E Levels and Respiratory Tract Infections in Children (School Collaboration 20223160A0463).

Data Availability Statement: Not applicable.

Acknowledgments: We would like to thank the editors and anonymous reviewers for their reviews and comments.

Conflicts of Interest: The authors declare no conflict of interest.

References

1. Kuppusamy, N.R.; Saidur, R.; Ghazali, N.N.N.; Mohammed, H.A. Numerical study of thermal enhancement in micro channel heat sink with secondary flow. *Int. J. Heat Mass Transf.* **2014**, *78*, 216–223. [[CrossRef](#)]
2. Ahmed, H.E.; Salman, B.H.; Kherbeet, A.S.; Ahmed, M.I. Optimization of thermal design of heat sinks: A review. *Int. J. Heat Mass Transf.* **2018**, *118*, 129–153. [[CrossRef](#)]
3. Wei, Z.; Jianjun, S.; Tao, N.; Chenbo, M.; Qiuping, Y.; Yuyan, Z. Structural optimization and heat transfer performance analysis of a cone-column combined heat sink. *J. Heat Transf.* **2020**, *142*, 044504. [[CrossRef](#)]
4. Datta, A.; Sharma, V.; Sanyal, D.; Das, P. A conjugate heat transfer analysis of performance for rectangular microchannel with trapezoidal cavities and ribs. *Int. J. Therm. Sci.* **2019**, *138*, 425–446. [[CrossRef](#)]
5. Japar, W.M.A.A.; Sidik, N.A.C.; Mat, S. A comprehensive study on heat transfer enhancement in microchannel heat sink with secondary channel. *Int. Commun. Heat Mass Transf.* **2018**, *99*, 62–81. [[CrossRef](#)]
6. Tuckerman, D.B.; Pease, R.F.W. High-performance heat sinking for VLSI. *IEEE Electron Device Lett.* **1981**, *2*, 126–129. [[CrossRef](#)]
7. Alihosseini, Y.; Azaddel, M.R.; Moslemi, S.; Mohammadi, M.; Pormohammad, A.; Targhi, M.Z.; Heyhat, M.M. Effect of liquid cooling on PCR performance with the parametric study of cross-section shapes of microchannels. *Sci. Rep.* **2021**, *11*, 16072. [[CrossRef](#)]
8. Liu, H.L.; Shi, H.B.; Shen, H.; Xie, G. The performance management of a Li-ion battery by using tree-like mini-channel heat sinks: Experimental and numerical optimization. *Energy* **2019**, *189*, 116150. [[CrossRef](#)]
9. Lan, C.; Xu, J.; Qiao, Y.; Ma, Y. Thermal management for high power lithium-ion battery by minichannel aluminum tubes. *Appl. Therm. Eng.* **2016**, *101*, 284–292. [[CrossRef](#)]
10. Radwan, A.; Ahmed, M.; Ookawara, S. Performance enhancement of concentrated photovoltaic systems using a microchannel heat sink with nanofluids. *Energy Convers. Manag.* **2016**, *119*, 289–303. [[CrossRef](#)]
11. Chen, L.; Deng, D.; Huang, Q.; Xu, X.; Xie, Y. Development and thermal performance of a vapor chamber with multi-artery reentrant microchannels for high-power LED. *Appl. Therm. Eng.* **2020**, *166*, 114686. [[CrossRef](#)]
12. Mohammed, H.A.; Gunnasegaran, P.; Shuaib, N.H. Numerical simulation of heat transfer enhancement in wavy microchannel heat sink. *Int. Commun. Heat Mass Transf.* **2011**, *38*, 63–68. [[CrossRef](#)]
13. Lin, L.; Zhao, J.; Lu, G.; Wang, X.D.; Yan, W.M. Heat transfer enhancement in microchannel heat sink by wavy channel with changing wavelength/amplitude. *Int. J. Therm. Sci.* **2017**, *118*, 423–434. [[CrossRef](#)]
14. Mohammed, H.A.; Gunnasegaran, P.; Shuaib, N.H. Influence of channel shape on the thermal and hydraulic performance of microchannel heat sink. *Int. Commun. Heat Mass Transf.* **2011**, *38*, 474–480. [[CrossRef](#)]
15. Chai, L.; Xia, G.; Zhou, M.; Li, J. Numerical simulation of fluid flow and heat transfer in a microchannel heat sink with offset fan-shaped reentrant cavities in sidewall. *Int. Commun. Heat Mass Transf.* **2011**, *38*, 577–584. [[CrossRef](#)]
16. Chai, L.; Xia, G.; Wang, L.; Zhou, M.; Cui, Z. Heat transfer enhancement in microchannel heat sinks with periodic expansion–contraction cross-sections. *Int. J. Heat Mass Transf.* **2013**, *62*, 741–751. [[CrossRef](#)]
17. Li, Y.; Wang, Q.; Li, M.; Ma, X.; Xiao, X.; Ji, Y. Investigation of Flow and Heat Transfer Performance of Double-Layer Pin-Fin Manifold Microchannel Heat Sinks. *Water* **2022**, *14*, 3140. [[CrossRef](#)]
18. Li, Y.F.; Xia, G.D.; Ma, D.D.; Jia, Y.T.; Wang, J. Characteristics of laminar flow and heat transfer in microchannel heat sink with triangular cavities and rectangular ribs. *Int. J. Heat Mass Transf.* **2016**, *98*, 17–28. [[CrossRef](#)]
19. Pan, Y.H.; Zhao, R.; Nian, Y.L.; Cheng, W.L. Numerical study on heat transfer characteristics of a pin–fin staggered manifold microchannel heat sink. *Appl. Therm. Eng.* **2023**, *219*, 119436. [[CrossRef](#)]
20. Feng, Z.; Hu, Z.; Lan, Y.; Huang, Z.; Zhang, J. Effects of geometric parameters of circular pin-fins on fluid flow and heat transfer in an interrupted microchannel heat sink. *Int. J. Therm. Sci.* **2021**, *165*, 106956. [[CrossRef](#)]
21. Alihosseini, Y.; Targhi, M.Z.; Heyhat, M.M. Thermo-hydraulic performance of wavy microchannel heat sink with oblique grooved finned. *Appl. Therm. Eng.* **2021**, *189*, 116719. [[CrossRef](#)]
22. Omri, M.; Smaoui, H.; Frechette, L.; Kolsi, L. A new microchannel heat exchanger configuration using CNT-nanofluid and allowing uniform temperature on the active wall. *Case Stud. Therm. Eng.* **2022**, *32*, 101866. [[CrossRef](#)]
23. Paramanandam, K.S.V.; Srinivasan, B. Heat transfer enhancement in microchannels using ribs and secondary flows. *Int. J. Numer. Methods Heat Fluid Flow* **2022**, *32*, 2299–2319. [[CrossRef](#)]
24. Japar, W.M.A.A.; Sidik, N.A.C.; Saidur, R.; Kamaruzaman, N.; Asako, Y.; Yusof, S.N.A. The effect of triangular cavity shape on the hybrid microchannel heat sink performance. *CFD Lett.* **2020**, *12*, 1–14. [[CrossRef](#)]
25. Karwa, R.; Sharma, C.; Karwa, N. Performance evaluation criterion at equal pumping power for enhanced performance heat transfer surfaces. *J. Sol. Energy* **2013**, *37*, 23–32. [[CrossRef](#)]
26. Webb, R.L. Performance evaluation criteria for use of enhanced heat transfer surfaces in heat exchanger design. *Int. J. Heat Mass Transf.* **1981**, *24*, 715–726. [[CrossRef](#)]

27. Pan, M.; Zhong, X.; Dong, G.; Huang, P. Experimental study of the heat dissipation of battery with a manifold micro-channel heat sink. *Appl. Therm. Eng.* **2019**, *163*, 114330. [[CrossRef](#)]
28. Taylor, B.N.; Kuyatt, C.E. *Guidelines for Evaluating and Expressing the Uncertainty of NIST Measurement Results*; US Department of Commerce, Technology Administration: Washington, DC, USA; National Institute of Standards and Technology: Gaithersburg, MD, USA, 1994.

Disclaimer/Publisher's Note: The statements, opinions and data contained in all publications are solely those of the individual author(s) and contributor(s) and not of MDPI and/or the editor(s). MDPI and/or the editor(s) disclaim responsibility for any injury to people or property resulting from any ideas, methods, instructions or products referred to in the content.